Experimental and numerical investigation on the performance of fluid pivot journal bearing in one-sided floating state

Mingyang Lou[a,b], Olivier Bareille[b], Wei Chen[a,*], Xing Xu[a]

[a] School of Mechanical Engineering Key Laboratory of Ministry of Education for Modern Design &Rotor-Bearing System, Xi'an Jiaotong University, Xi'an, Shaanxi, 710049, China
[b] Laboratoire de Tribologie et Dynamique des Systemes, Ecole Centrale de Lyon, 36 Avenue Guy de Collongue, 69134, Ecully Cedex, France

ARTICLE INFO

ABSTRACT

The performance of fluid pivot journal bearing (FPJB) in the one-sided floating state is studied experimentally and numerically. The effects of pressure tap diameter and recess area ratio on recess pressure, floating height and load-carrying capacity of the bearing are presented. Constant load and various speeds are studied in test and numerical calculations. The results show that the recess pressure increases from 448 to 1800 RPM and keep constant from 2242 to 3300 RPM. Pad tilting angle almost has no change with the increase of speed. The larger pressure tap diameter leads to an increase of bearing capacity. The larger recess area ratio results in the smaller recess pressure and the bearing capacity remains constant.

1. Introduction

Nowadays high-speed and heavy-load have become a dominating development trend of modern rotating machinery. These conditions often have rotors that pass through one or two bending critical speed as the machine is accelerated to operating speed. Due to the existence of rotor unbalance, shaft fluctuation, lubricant contamination and so on, it is easy for rotating machinery to vibrate and thus transmit force to pedestal when running at high speed. In order to ensure the safe operation of equipment, the vibration of the shaft must be controlled.

Compared with other types of fluid-film bearings, tilting-pad journal bearings is of high stability on account of each pad free to rotate around its pivot and do not support a moment [1]. This made tilting-pad journal bearing become an optimization fluid-film bearing for most engineering application. However, due to its low damping coefficient, the rotor may have large amplitude when passing through the critical speed and the oil film instability occurs occasionally.

In order to reduce the rotor amplitude and the force transmitted to the bearing support structure, many designs and techniques have been attempted. An active lubrication design for the tilting-pad journal bearing was introduced by Santos [2]. In this design, the high-pressure oil is injected directly into the bearing clearance, passing radial holes drilled across the pad. By modifying the injection pressure during the bearing operation, the hydrodynamic pressure distribution can be varied, thus the bearing performance can be changed, which results in a

modification of the system behavior. The development history of tilting-pad journal bearing with controllable lubrication was summarized by Varela [3].

Another type of active tilting-pad journal bearing using piezo-electric actuators to radially move the pivots of the pads of a tilting-pad journal bearing was described by Deckler and co-workers [4,5]. In this design, a simulation based on the Reynolds equation was used to calculate the steady and transient-state motions of the shaft and the pads in the bearing to record the real-time distribution of the oil film thickness and pressure of each pad. Meanwhile, a feedback control was designed to make the simulation accommodate the actuated radial motion of the pad pivot so as to achieve the purpose of vibration control. Further, flexible pivot [6] fabricated by wire electric discharge machining process is more and more used in tilting pad journal bearing to avoid the drawbacks of conventional tilting pad journal bearing.

Additionally, introducing a damper into the rotor-bearing system also is an attempt to cope with the excessive rotor vibration in rotating machinery. At present, magnetorheological damper, mechanical structure damper, squeeze-film damper and their combination are widely used in engineering practice. Magnetorheological damper [7–12] using magnetorheological liquid, a kind of completely reversible and controllable fluid, shows obvious nonlinear rheological effect under the action of an external magnetic field. The damper made of magnetorheological liquid can adjust the intensity of the magnetic field according to the external vibration and generate the corresponding

---

* Corresponding author.
E-mail address: lmy87521175@stu.xjtu.edu.cn (W. Chen).

Nomenclature

A_{ratio}	Recess area ratio
C_b	Assembling clearance, $R_b - R$
C_p	Radius clearance, $R_p - R$
D	Journal diameter, $D = 2R$
D_t	Pressure tap diameter
e	Eccentricity
F_x	Hydrodynamic resultant force in the horizontal direction
F_y	Hydrodynamic resultant force in the vertical direction
h_d	Hydrodynamic oil film thickness
H_d	Dimensionless hydrodynamic oil film thickness
h_s	Hydrostatic oil film thickness
H_s	Dimensionless hydrostatic oil film thickness
l	Recess length in axial (λ) direction
L	Bearing or pad length
m_p	Geometrical preload ratio, δ/C_p
O	Bearing center
O_p	The curvature center of the inner surface of the pad
O_r	Journal center
O_z	The curvature center of the outer surface of the pad
p_d	Hydrodynamic film pressure
P_d	Dimensionless hydrodynamic film pressure
p_s	Hydrostatic film pressure
P_s	Dimensionless hydrostatic film pressure
P_r	Recess pressure
P_{rmax}	Maximum recess pressure
P_{in}	Oil inlet pressure
Q_d	Hydrodynamic flow
Q_h	Pressure tap flow

Q_s	Hydrostatic flow
R	Journal radius
R_b	Assembly radius
R_p	Radius of curvature of the inner surface of the bearing pad
R_z	Radius of curvature of the outer surface of the bearing pad
t	Pad thickness
T_d	Resultant hydrodynamic torque
T_s	Resultant hydrostatic torque
T_{in}	Oil inlet temperature
U_n	Projection of shaft tangential velocity on the outer normal direction around the pressure tap
W	Applied load
α	Tilting angle
β	Pad arc
δ	Preload
ε	Eccentricity ratio, e/C_p
θ	Attitude angle
Λ	Titling angle coefficient, $R_p\alpha/C_p$
Λ_{max}	Maximum tilting angle coefficient
μ	Lubricant dynamic viscosity
Φ	Coordinate in circumferential direction
Φ_{MC}	Position angle of pad manufacture center
Φ_{TC}	Position angle of pad tilting center
Φ_s	Position angle of pad start edge
Φ_e	Position angle of pad end edge
Φ_{rs}	Position angle of recess start edge
Φ_{re}	Position angle of recess end edge
λ	Coordinate in the axial direction
i	Pad subscribe

damping force to suppress the vibration of the equipment. Mechanical structural damper reduces the vibration of equipment through the damping characteristics of the material itself. The materials used in mechanical structural dampers are diverse, including metal materials [13,16–18], epoxy materials [16,18], rubber [14,15], polytetra-fluoroethylene (Teflon) [17,18], composite materials [18] and so on.

Squeeze oil film damper (SFD) has the characteristics of simple structure, less space occupied, easy to manufacture and remarkable effect of vibration reduction, so squeeze oil film damper has become a typical design for modern gas turbine engines [19]. In its simplest form, squeeze-film damper consists of a fluid-filled annular cavity sur-rounding the outer face of a fluid-film bearing house. A comprehensive review of the relevant analytical and experimental work conducted on SFD was provided by Adilleta and Della Pietra [20,21]. San Andrés and co-workers discuss more recent SFD experimental research based on grooved SFD [22–24] and more realistic operating condition such as lubricant cavitation and air entrainment [25,26].

Fluid pivot journal bearing as the improved design of tilting pad journal bearing has been employed in industry for a while expecting to increase the vibration attenuation and reliability demands for advanced machinery such as high-speed compressors, gas/steam turbines and motor spindle etc.

In 1970, the prototype of fluid pivot journal bearing was proposed and the operating principle of this bearing design was clarified by L. W. Hollingsworth [27]. According to years wide-ranging of research, testing and service experience, in 1977, the configuration of the bearing is improved in the position of recess and pad stop to obtain a better floating state of the pad by L. W. Hollingsworth [28]. Later on, an improvement of pad outer face shaped from cylinder to sphere is de-signed in 2000 by G. A. Messmer and L. A. Branagan [29] to allow the bearing to support the shaft during both radial motion and axial mis-alignment without compromising the performance of the hydrostatic film. The development history, as well as static and dynamic

performance of fluid pivot journal bearing, has been presented in Ref. [30]. Based on the design improvement of the pad, fluid pivot journal bearing owns many merits. The self-generated hydrostatic oil film dis-tributed over the outer face of pad tend to oppose the hydrodynamic pressure distribution leading to reduced pad mechanical and thermal distortion [31]. Because of the elimination of any type of mechanical pivot, the whole bearing can be configured more compact and the pivot fretting can be avoided to obtain a more stable bearing performance [32]. Furthermore, the design of supplying oil directly from a hole in the bearing shell through the pad to spreader grooves improve bearing load capacity and also lead to a reduction in power loss [33–35]. Be-sides, the significant improvement of rotor dynamic performance over a certain frequency range is proved by A. V. Harangozo and T. A. Sto-larski by comparing the fluid pivot journal bearing with an ordinary bearing [36].

Although fluid pivot journal bearing has many advantages, it is a complicated design work to obtain the full floating state of a pad. By using eddy current probes, the full floating state has been observed repeatedly [30]. However, over a certain speed and load range, a well-designed fluid pivot journal bearing also can in a state of one-sided floating and bearing performance thus changes dramatically. The floating state not only depends on the operation condition but also depends on the design parameters of the bearing. It is possible to state that between the full floating and no floating state, the one-sided floating state is a necessary path from the speed-up stage to the steady-state stage, which should be paid enough attention. However, to the best of the authors' knowledge, the corresponding works on fluid pivot journal bearing in the state of one-sided floating are hardly reported. Moreover, because the pad of fluid pivot journal bearing has more freedom, conducting tests is a necessary and effective means to de-termine the posture of the pad in fluid pivot journal bearing.

This paper reports the results of test studies on the performance of a fluid pivot journal bearing with the load pad of the bearing stay in the

one-sided floating state, the corresponding full-scale test rig is built, the pressure and temperature of recess and the floating height of pad are measured to determine the floating state of the pad. At the same time, different pressure tap diameters and recess area ratios were tested to study the effect of these two design parameters on bearing performance. Comparison between test results and numerical calculations is made, the validity of analysis is confirmed.

2. Test rig

Fig. 1 shows the tested fluid pivot journal bearing, it is a load on pad (LOP) bearing with 3 pads. Fig. 2 shows the pad of the fluid pivot journal bearing, the inner surface of the pad is cast with Babbitt metal (ZSnSb11Cu6) to protect the pad from wear. Table 1 lists the design specification of the bearing.

Fig. 3 shows the longitudinal section of the inverted test rig. Both ends of the test rotor are supported with two 152 mm diameter five-pad tilting-pad journal bearings. The tested rotor is driven by a $250Kw$ AC motor through a gear box and a diaphragm coupling. The flexibility of the coupling can control the vibration of the motor transmitting through it to the shaft.

The test bearing is rigidly fixed to bearing house, and the bearing house is supported in the middle of the shaft with a loading support plate which is pulled by four rods connecting the plate and air bellow in the vertical direction. A static load is applied by filling with compressed air into the air bellow. The applied static load is a function of the pressure of compressed air and the diameter of air bellow. An increase of $0.1MPa$ correspond to an increase vertical load of $6800N$, the maximum applied static load is $50000N$. Because of the thin wall of the air bellow, the stiffness in the axial direction is smaller resulting in a smaller additional joint stiffness.

3. Measuring method

Fig. 4 (a) (b) shows the displacement measurement of the pad. Four eddy current probes (A, B, C, D) for each pad($i = 1,2,3$) are fixed on the bearing house by thread with their axis being parallel to the radial direction of corresponding measuring point on each pad for measuring the floating height at each measuring point.

Pressure and temperature data are recorded by installing pressure sensors SP, i and thermocouples ST, i under each pad($i = 1,2,3$), on the same axis and both sides of the bearing. As Fig. 5 shows, the measuring hole on the end face of bearing house connect with the recess through an inner passage, thus the measurement of pressure and temperature at the measuring hole can truly reflect the actual value of pressure and temperature in recess.

Absolute displacements of the bearing house in horizontal and vertical directions are measured by two eddy current probes AX and AY. In order to detect the relative displacement of the bearing house to the shaft, another two probes RX and RY are arranged to measure the motion of the shaft in the horizontal and vertical direction as indicated in Fig. 6. In this way, the relative and absolute displacements of the bearing house, as well as the shaft locus, are obtained.

Inlet and outlet oil temperatures are measured by the thermocouples inside the oil supply pipe and oil discharge pipe. The tests are performed using the ISO VG 68 turbine oil, with a supply temperature ranging from 42°C to 48°C. Oil flow rate is measured by the glass tube flowmeter on the oil supply pipe. Before the test, the linearity and zero points of sensors are checked.

The main parameters of sensors are listed in Table 2 and the photographic view of the test rig and test apparatus is shown in Fig. 7.

The experimental test rig allows the evaluation of the static and dynamic characteristics of journal bearing from run-up to run-down phase by varying the static load, rotating speed and lubricant parameters. In the present test, the test procedure including a constant speed operating at 2000 RPM and step up multi-speed operating at 448,

1073, 1800, 2242, 2730 and 3300 RPM is detailed in Fig. 8.

4. Numerical model

According to the operating characteristics and the floating state of fluid pivot journal bearing, the one-sided floating FPJB model was derived. Fig. 9 shows the bearing operation schematic in the one-sided floating state, comparing with the full floating state, the trailing edge of the pad floats and the bole (connecting bearing house and each pad) near the leading edge of the pad is taken as the tilting center.

According to the analyses above, the geometry of the fluid pivot journal bearing and the corresponding coordinate system is established as shown in Fig. 10. Considering the static performance of bearing, Reynolds equation governing the steady, laminar incompressible flows in hydrodynamic oil film in dimensionless form is given as follows [39]:

$$\frac{\partial}{\partial\Phi}\left(H_d^3\frac{\partial P_d}{\partial\Phi}\right) + \left(\frac{D}{L}\right)^2\frac{\partial}{\partial\lambda}\left(H_d^3\frac{\partial P_d}{\partial\lambda}\right) = \frac{\partial H_d}{\partial\Phi} \tag{1}$$

And in hydrostatic oil film can be written as:

$$\frac{\partial}{\partial\Phi}\left(H_s^3\frac{\partial P_s}{\partial\Phi}\right) + \left(\frac{2R_z}{L}\right)^2\frac{\partial}{\partial\lambda}\left(H_s^3\frac{\partial P_s}{\partial\lambda}\right) = 0 \tag{2}$$

Neglecting the elastic and thermal deformation of the bearing and journal, the corresponding oil film thickness in hydrodynamic oil film can be expressed as:

$$h_{d,i} = C_p - \delta\cos(\Phi_{MC,i} - \Phi) + e\cos(\Phi - \theta) + R_p\,\alpha_i\sin(\Phi_{TC,i} - \Phi) \tag{3}$$

Its non-dimensional form:

$$H_{d,i} = 1 - m_p\cos(\Phi_{MC,i} - \Phi) + \varepsilon\cos(\Phi - \theta) + \Lambda\sin(\Phi_{TC,i} - \Phi) \tag{4}$$

Where: $m_p = \delta/C_p$, $\varepsilon = e/C_p$, $\Lambda = (R_p\,\alpha_i)/C_p$.

In a similar way, the thickness of hydrostatic oil film can be expressed as:

$$h_{s,i} = -R_p\,\alpha_i\sin(\Phi_{TC,i} - \Phi) \tag{5}$$

Its non-dimensional form:

$$H_{s,i} = -\Lambda\sin(\Phi_{TC,i} - \Phi) \tag{6}$$

When the bearing is operated under a certain steady state, neglecting the misalignment between shaft and bearing, the maximum tilting angle can be derived as:

$$\Lambda_{max,i} = \sqrt{1 + (\varepsilon\sin(\Phi_{TC,i} - \theta))^2 - \varepsilon^2 - m_p^2 + 2\varepsilon m_p\cos(\Phi_{MC,i} - \theta)}$$
$$- \varepsilon\sin(\Phi_{TC,i} - \theta) \tag{7}$$

In steady state, the convergence wedge between the shaft and the

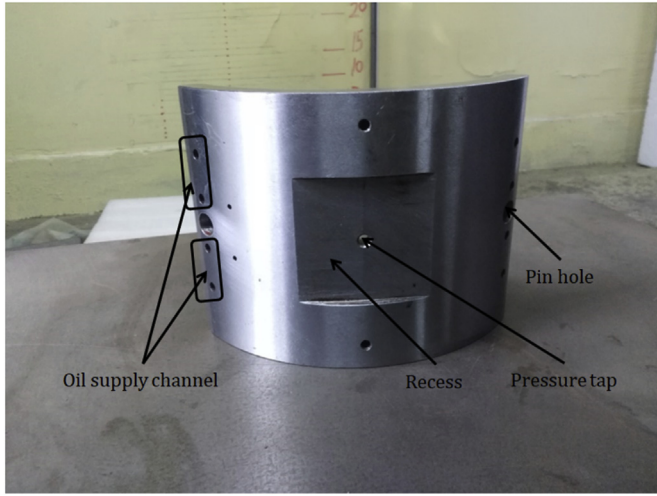**Fig. 1.** Fluid Pivot Journal Bearing (Endplates are not shown).

Fig. 2. Pad of fluid pivot journal bearing.

Table 1
Specification of the test bearing.

Journal radius, R/ mm	100
Bearing length, L/ mm	150
Number of pads, N_p/$-$	3
Pad thickness, t/ mm	14.91
Radius of curvature of the inner surface of the bearing pad, R_p/ mm	100.21
Radius of curvature of the outer surface of the bearing pad, R_z/ mm	115
Assembly radius, R_b/ mm	100.09
Geometrical preload ratio, m_p/$-$	0.57
Pad arc, β/deg/deg.	114
Position angle of pad manufacture center, Φ_{MC}/deg.	60, 180, 300
Pressure tap diameter, D_t/ mm	4/6/8
Recess area ratio, A_{ratio}/$-$	0.18/0.21/0.24
Oil inlet temperature, T_{in}/°C	45
Oil inlet pressure, P_{in}/MPa	0.1

inner face of pad forms the hydrodynamic oil film, by tapping off a portion of the hydrodynamic oil flow to pressurize the recess on the back of each pad, the hydrostatic oil film is created. For a prescribed bearing parameter and operating condition, the pad reaches the one-sided floating state. This process involves:

(1) The flow equilibrium between the flow from hydrodynamic oil film to pressure tap Q_h and the flow discharging from hydrostatic oil film Q_s, namely $Q_h = Q_s$.

The flow into the pressure tap can be expressed as a closed curve integral:

$$Q_h = \oint_\Gamma \left(\frac{hU_n}{2} - \frac{h^3}{12\mu} \frac{\partial p_d}{\partial n} \right) ds \tag{8}$$

Where, U_n is the projection of shaft circumference velocity on the outer normal direction around the pressure tap, h is the oil film thickness around the pressure tap edge.

The flow discharged from the hydrostatic oil film to four directions:

$$Q_s = Q_{sx}|_{\Phi=\Phi_s} + Q_{sx}|_{\Phi=\Phi_e} + Q_{sz}|_{z=L/2} + Q_{sz}|_{z=-L/2} \tag{9}$$

Where,

$$Q_{sx} = \int_{-\frac{L}{2}}^{\frac{L}{2}} q_{sx} dz = -\int_{-\frac{L}{2}}^{\frac{L}{2}} \frac{h_s^3}{12\mu} \frac{\partial p_s}{\partial x} dz \tag{10}$$

$$Q_{sz} = \int_{\varphi_s}^{\varphi_e} q_{sz} dx = -\int_{\varphi_s}^{\varphi_e} \frac{h_s^3}{12\mu} \frac{\partial p_s}{\partial z} dx \tag{11}$$

(2) The torque equilibrium between the resultant torque integrated by hydrodynamic pressure M_d and the resultant torque integrated by hydrostatic pressure M_s, namely $M_d = M_s$.

The torque results from the hydrodynamic pressure can be written as:

$$M_d = -\frac{RR_z L}{2} \int_{\Phi_s}^{\Phi_e} \int_{-1}^{1} p_d \sin(\Phi_s - \Phi) d\lambda d\Phi \tag{12}$$

While the torque resulting from the hydrostatic pressure comes from two integrals, the torque integrated by the recess pressure M_{sr} can be written as:

$$M_{sr} = -\frac{R_z^2 L}{2} \int_{\Phi_{rs}}^{\Phi_{re}} \int_{-l/L}^{l/L} p_s \sin(5\pi/18) d\lambda d\Phi \tag{13}$$

Where $5\pi/18$ is the angle from the line of the pad tilting center $\Phi = \Phi_{TC}$ to the line of the pad manufacturing center $\Phi = \Phi_{MC}$ as Fig. 10 shows.

The torque integrated by pressure out of the recess M_{sor}, can be expressed as follows:

Fig. 3. Schematic of the test rig.

1 AC motor
2 shaft coupling
3 gearbox
4 diaphragm coupling
5 shaft
6 support bearing (TPJB)
7 bearing house
8 supporting platform
9 connecting rod
10 pressure transducer
11 bearing house
12 test bearing (FPJB)
13 air bellow
14 loading support plate
15 axial positioning disc
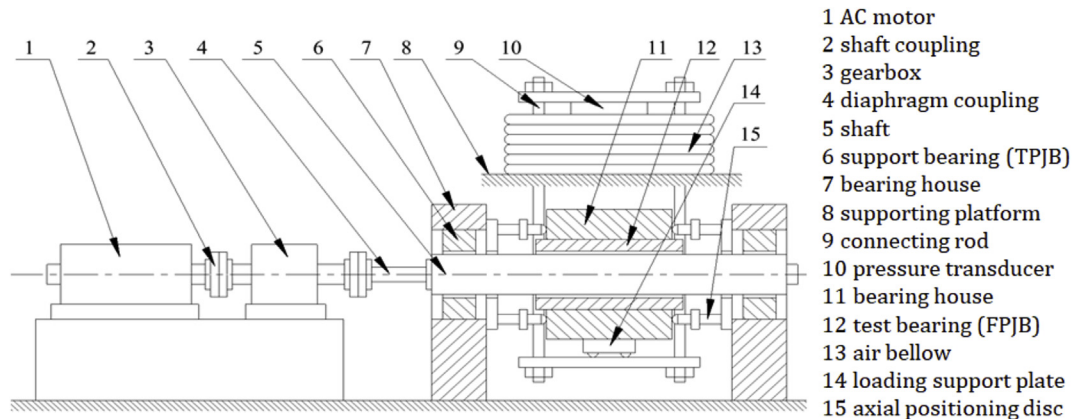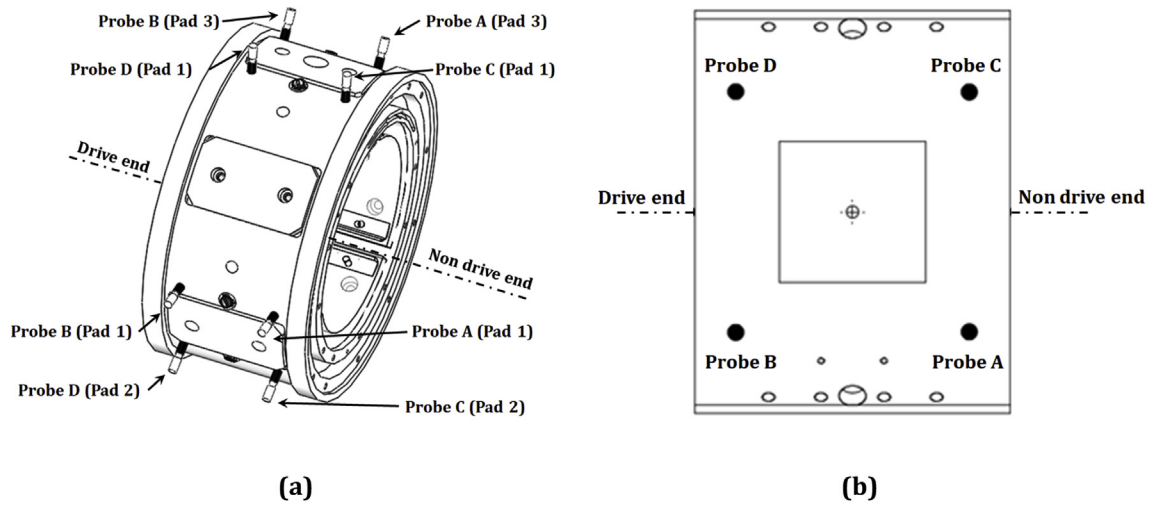
Fig. 4. Location of eddy current probe for measuring pad displacement.
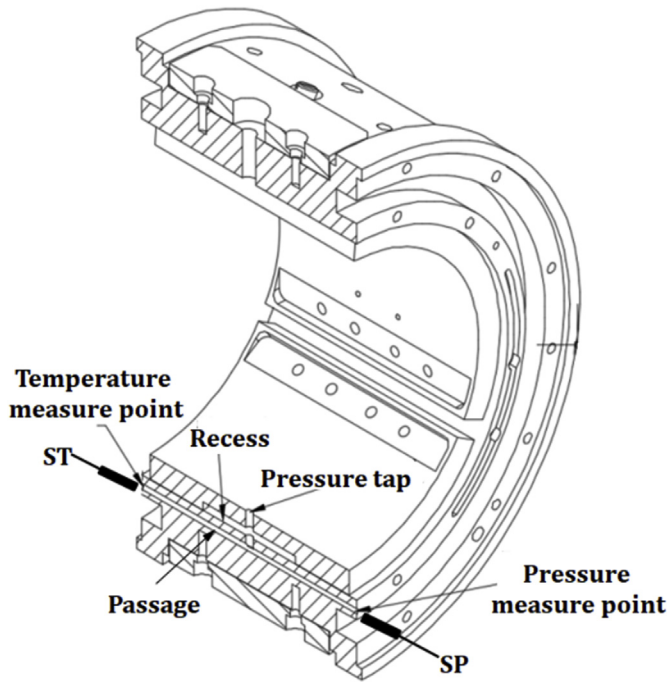

Fig. 5. Location of pressure sensors and thermocouples.
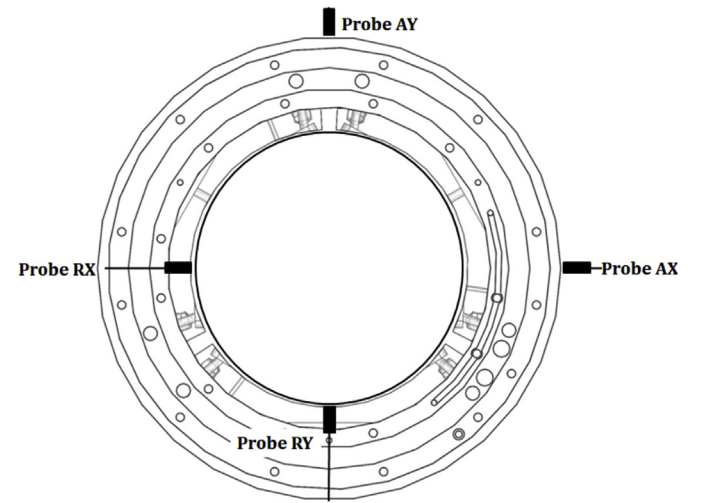

Fig. 6. Location of eddy current probe for measuring shaft displacement.

Table 2
Main parameters of sensors.

Sensor	range	Sensitivity	Accuracy
Eddy current proximity (Probe $A/B/C/D$, $i = 1 \sim 3$) (Probe $AX/AY/RX/RY$)	0.1–0.6 mm	32 V/mm	1.0% NE
Pressure ($SPi = 1 \sim 3$)	0–70 BAR	14 BAR/V	0.5% FS
Temperature ($ST, i = 1$–3)	0 $\sim 200°C$	20$°C/V$	0.5% FS

$$M_{sor} = \frac{R_z^2 L}{2} \left(\int_{\Phi_s}^{\Phi_{rs}} \int_{-1}^{1} p_s \sin(\Phi_s - \Phi) d\lambda d\Phi + \int_{\Phi_{re}}^{\Phi_e} \int_{-1}^{1} p_s \sin(\Phi_s - \Phi) d\lambda d\Phi + \right.$$

$$\left. \int_{\Phi_{rs}}^{\Phi_{re}} \int_{-1}^{-\frac{l}{L}} p_s \sin(\Phi_s - \Phi) d\lambda d\Phi + \int_{\Phi_{rs}}^{\Phi_{re}} \int_{l/L}^{1} p_s \sin(\Phi_s - \Phi) d\lambda d\Phi \right)$$

$$\tag{14}$$

Where Φ_s, Φ_e represent the angle of pad start edge and pad end edge, Φ_{rs}, Φ_{re} represent the angle of the recess start edge and the recess end edge, l represents the recess length in λ direction.

(3) The applied load is equal to the load-carrying capacity of the bearing, namely $W = F_y$. The load-carrying can be calculated as following:

$$F_y = \sum_{i=1}^{3} F_{yi} \tag{15}$$

$$F_{yi} = \frac{RL}{2} \int_{\Phi_s}^{\Phi_e} \int_{-1}^{1} p_d \cos\Phi d\lambda d\Phi \tag{16}$$

(4) The resultant force is vertical, namely, $F_x = 0$.

$$F_x = \sum_{i=1}^{3} F_{xi} \tag{17}$$

$$F_{xi} = \frac{RL}{2} \int_{\Phi_s}^{\Phi_e} \int_{-1}^{1} p_d \sin\Phi d\lambda d\Phi \tag{18}$$

To obtain the static characteristics of FPJB, the Reynolds equation is discretized by the Finite Difference Method (FDM) and solved iteratively by Newton-Raphson root-finding algorithm. The pressure at all edges of the pad is equal to zero and negative film pressure is not
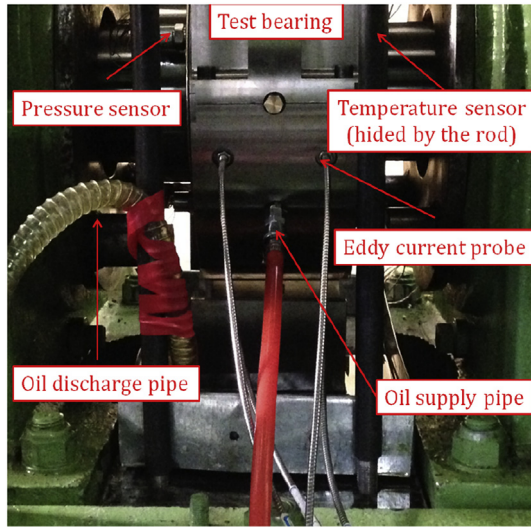
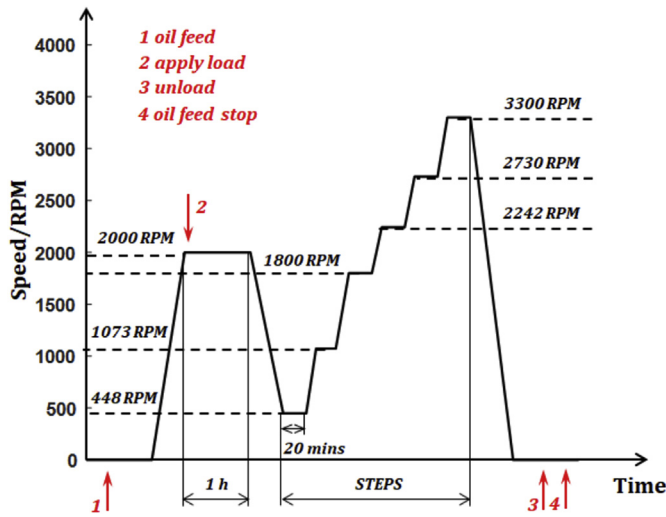**Fig. 7.** Photographic view of the test rig and test apparatus.
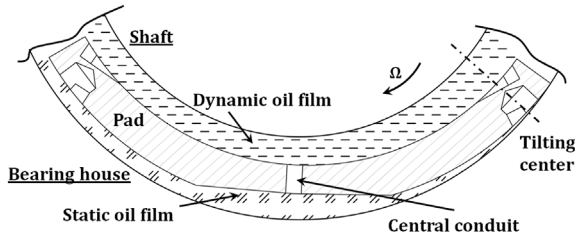

Fig. 8. Test procedure.

Fig. 9. Bearing operation schematic.

permitted. When negative film pressure occurs during the course of calculations, the negative value is replaced with zero pressure and the calculations are continued. The pressure and pressure gradient are zero at film rupture. Neglecting the cavitation effect, the following classic Reynolds boundary conditions are used:

$$
\begin{aligned}
&P(\Phi, \pm L/2) = 0 && \text{at side edges} \\
&P(\Phi_s, \lambda) = P(\Phi_e, \lambda) = 0 && \text{at leading and trailing edge} \\
&(\partial P(\Phi, \lambda))/\partial \Phi = 0 && \text{at ending edge}
\end{aligned} \tag{19}
$$

Because of the high rotating speed leads to a high temperature in lubricant which dramatically changes the lubricant's viscosity and
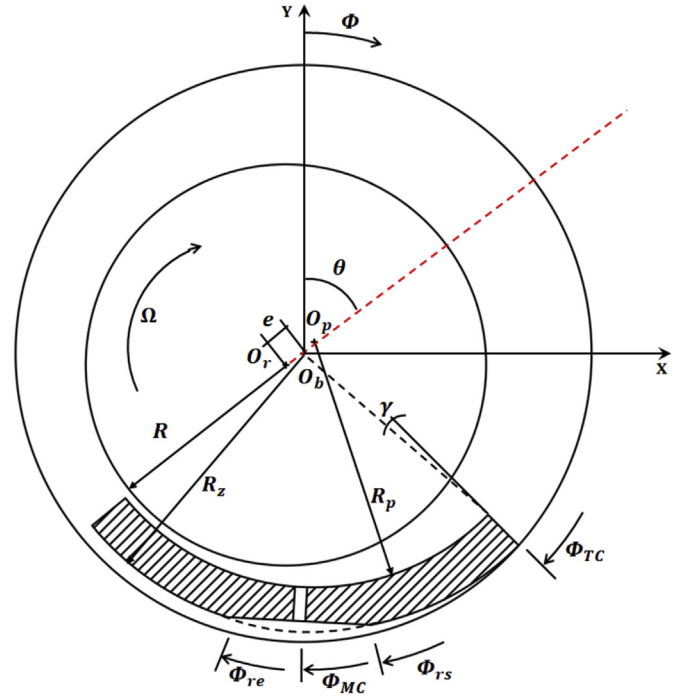
Fig. 10. Geometry of one-sided floating FPJB and coordinate system.

lubrication condition, different viscosity should be used. To obtain the lubricant viscosity corresponding to the specific temperature, the average recess oil temperature of each pad is calculated by averaging the temperature data at each different speed. The temperature is measured by thermocouples every 4 min when the shaft is operated at different speeds. Each speed lasts for 20 min to make the bearing reach a steady state. The results for different speeds are shown in Fig. 11. In general, the recess temperature increases gradually with the increase of speed for all pads. It can be seen that over the speed range of the test, the recess oil film temperature of the load pad (pad 1) is the highest, while the recess temperature of pad 2 is higher than pad 3.

However, in order to obtain greater safety margins in calculation and design, only the loaded pad temperature is used. Furthermore, for a more accurate evaluation, Eq. (20), namely the Vogel equation, is considered to calculate the viscosity at different oil temperature [37,38]:
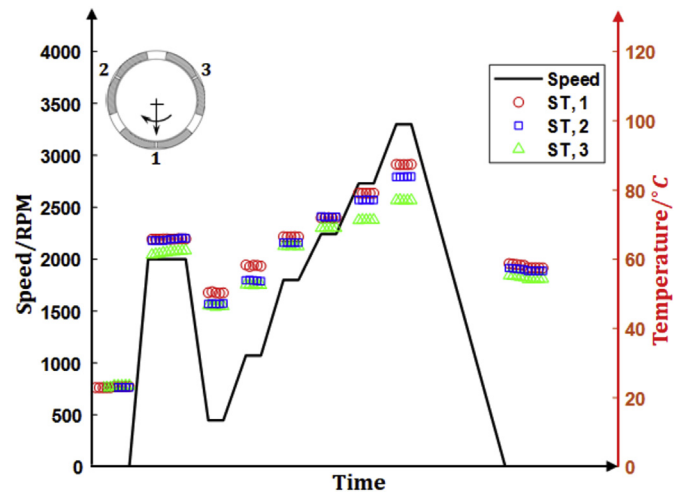
Fig. 11. Recess oil film temperature for different speed
$D_t = 6\,mm, A_{ratio} = 0.21, W = 6800N$

$$\mu_0 = ae^{\frac{b}{(T_A - c)}} \tag{20}$$

Where a, b, c are constant, T_A is the absolute temperature, μ_0 represents the dynamic viscosity.

This viscosity is used in numerical calculation corresponding to a specific temperature at different speed. It should be noticed that to used Vogel equation to approximate viscosity at a specific temperature, three viscosity measurements at different temperature are needed to determine the three constants. Fig. 12 shows the relationship between the temperature and viscosity based on the Vogel equation, which shows a good agreement with the benchmark value [37].

Each pad is divided into 100×100 elements. It is verified that the more refined mesh almost does not affect the results. For each iteration including oil film pressure, flow equilibrium, torque equilibrium and force equilibrium (magnitude and direction of the force), a relative error of convergent tolerance 10^{-6} is preset to deal with terminating the corresponding iteration [40]. When all iterations stop, oil film pressure in a steady state is obtained to calculate the static characteristics of fluid pivot journal bearing. However, if the rotor operates at a lower speed (448 *RPM*) and the pad is not floated, the stop criterion of maximum loop threshold (100) is set to avoid the infinite iteration. Fig. 13 shows the flowchart of the procedure.

5. Results and discussions

5.1. Determination of one-sided floating state and oil film distribution

By monitoring the displacement and pressure measuring points, the one-sided floating state of the load pad is determined, while the upper two pads show a no floating state according to the corresponding data. Fig. 14 shows the displacement data of the one-sided floating state of the load pad. The left ordinate represents the rotating speed of shaft corresponding to the solid line and the right ordinate represents the displacement measurement of each measuring point on the pad.

Generally, before and after oil supply, the floating heights of each measuring point almost have no change. The displacement measurements of probe C&D show positive floating heights and the other two (probe A&B) show negative ones, which proves the existence of a tilting angle of the load pad, thus indicates a one-sided floating state. Meanwhile, we also noticed that the floating heights at the rotating speed of 448 *RPM* show an opposite result indicating a no floating state at this speed, through which we can also determine the pad act as a fixed-lobe at this speed.

Focusing on the higher speed of 1073, 1800, 2242, 2730 and 3300 *RPM* in multi-speed stage, despite the displacement measurements of all measuring points decrease with the increase of speed, a constant distance can be found between the displacement measurements of probe C &D and the displacement measurement of probe A&B, namely a constant tilting angle of the pad with the increase of rotating speed. It also can be clearly seen that the floating measurements at all displacement measuring points show downward translation as operating speed increases.

On the one hand, the gradually decreased negative displacement measurements of probe A&B can explain the fact that there is no rigid contact between the pad and the bearing house for the range of the speed, that is to say, a squeeze-film exist in the clearance formed by the pad and the bearing house. On the other hand, considering the test procedure, lubricant oil was supplied before each test and meanwhile, the endplates were also used, which provide conditions for the formation of the squeeze-film.

Pressure distribution was obtained by numerical calculations once the one-sided floating state was determined. Fig. 15 (a), (b) presents the hydrodynamic and hydrostatic pressure oil film distribution under the prescribed design parameters and operating conditions.

In Fig. 15(a), a pressure drop presents in the center of the

hydrodynamic pressure distribution due to the existence of pressure tap, because of the one-sided floating state, the position of the minimum oil film moves backwards, the divergent region of the oil film enlarges and no hydrodynamic pressure produce here. The peak of the distribution reaches up to 1.5*MPa*, while in the center of the distribution, the pressure drop to 0.6 *MPa*. As Fig. 15(b) shows, the dropped pressure (0.6 *MPa*) distribute evenly in recess, the discharge from the clearance between the pad and bearing house formed a concave distribution at shaft rotating direction and axial direction, because the oil film is squeezed in the tilting center region, an arc distribution show up.

5.2. Effect of pressure tap diameter

In order to ensure any comparisons in future be conducted are effective, it is useful to look back the entire pad floating quality in Fig. 14, the displacement measurements of the pad are important in that they show if the pad is aligned with the shaft or if there is edge skew loading that can distort comparisons and lead to erroneous conclusions. The symmetric pattern of Fig. 14 indicates good axial alignment between the load pad and shaft. With this assurance, the performance for different design parameters of the pad can be compared.

According to the design of the pad, a passage extending from the recess to the end face of bearing house connects to pressure tap allows us could install pressure and temperature sensor on the end face of bearing house and monitor recess pressure and temperature easily.

Three sets pads with different pressure tap diameters are tested to study the effect of pressure tap on bearing performance. The values of pressure tap diameter are shown schematically in Fig. 16. Other than that, the rest design parameters of the pad are identical.

As shown in Fig. 17, the left ordinate represents the speed of the shaft and the right ordinate represents the test and calculation results of recess pressure. In terms of the test results, for a certain pressure tap diameter, at lower rotating speed from 448 to 1800 *RPM*, the recess pressure increases gradually, and then keep constant at higher rotating speeds from 2242 to 3300 *RPM*. As to calculation results, similar trends and magnitudes can be seen from 1800 to 3300 *RPM*, the numerical program shows an infinite loop at 448 *RPM* because of the no-equilibrium of the flow rate. The values of recess pressure show no difference when different diameters are tested. Numerical calculations show good agreement with the test results.

Though a non-zero value of recess pressure at 448 *RPM* is detected in all three sets, while the corresponding displacement data show there is no any floating at all displacement measure points (Figs. 14 and 18),
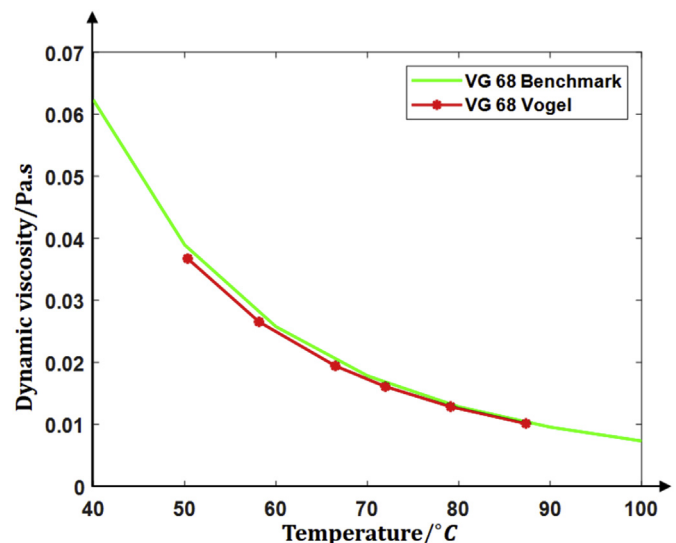
Fig. 12. Temperature-viscosity relationship of the lubricant (ISO VG 68).
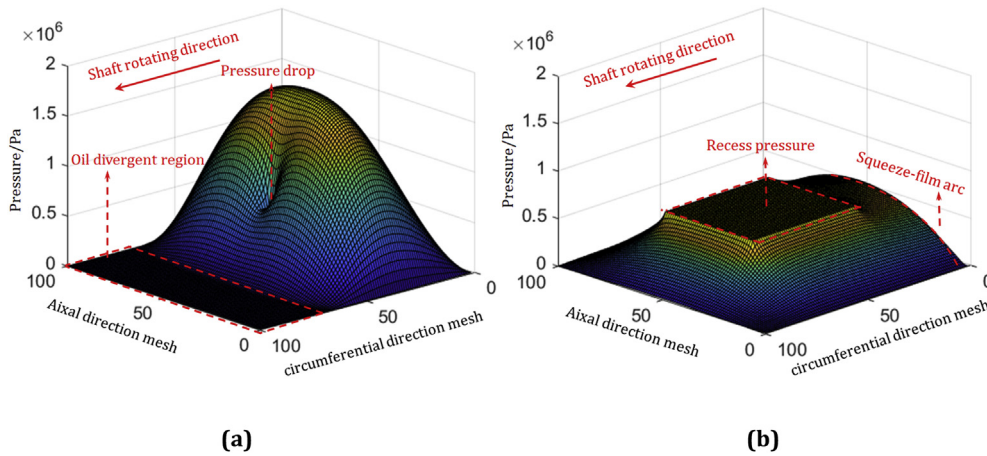
Fig. 13. Flowchart of the numerical calculation.

Fig. 14. Floating height of displacement measure points of the lower pad $D_t = 6mm$, = 0.21, = 6800N.

put it all together, the explanation of no-floating state resides with the fact that the lower speed caused an insufficient pressure in recess for one-sided floating state.

Howeve, the pressure tap diameters affect the tilting angle of the pad a lot. As shown in Fig. 18, the horizontal axis represents the step-up multi-speed stage from 448 to 3300 *RPM*, the vertical axis represents the average floating heights of displacement measuring points C&D. The discrete points are the average of the data recording by eddy current probe C&D, namely:

$$Average\ floating\ height = \frac{1}{2}\left(vaule(Probe\ C) + value(Probe\ D)\right) \tag{21}$$

In order to merely compare the effect of the pressure tap diameter on the tilting angle of the pad, these data exclude the downward translation caused by the compressed hydrostatic oil film. The solid lines are floating heights obtained by numerical calculations. Similarly, the numerical results are not given at 448 *RPM* because of the no-equilibrium of flowrate.

In terms of the test results, the average floating heights show the negative value at 448 *RPM* in all three sets, it has been proved repeatedly in the test that the pad is not in the one-sided floating state, thus act as a fixed-lobe at this speed. Paying more attention at higher rotating speeds, although the average floating heights show an inconsistency at 1073 *RPM*, the trends can be found that the average floating height does not change as speed increases and the larger tap diameter results in a larger average floating height.

This trend can be explained by flowrate equilibrium, the larger tap diameter responds to more flow rate driven from hydrodynamic oil film into pressure tap, the higher average floating height increases the hydrostatic discharge flow rate to obtain the flow equilibrium with the increased tap flow rate. Similar trends, but of different magnitudes, can be seen in numerical calculation. Generally, the test and numerical results agree well with each other in $D_t = 4mm$ set, the larger difference about 12 um occurred in the $D_t = 6mm$ set and the largest difference about 20um occurred in the $D_t = 8mm$ set. Recalling the measuring process in the test, this discrepancy is probably due to measurement error. When the pad reaches the one-sided floating state at a certain speed, the axis of eddy current probe will no longer be parallel with the radial direction of the pad at the corresponding measuring points, which consequently results in a larger measure value than the true value. As a result, larger average floating height causes a larger discrepancy between the test and numerical results. This is the reason why the discrepancy in the $D_t = 8mm$ set is larger than that in the $D_t = 6mm$ set, and that quite small in the $D_t = 4mm$ set.

Furthermore, the change of average floating height responds to the change of pad tilting angle, which consequently leads to the change of bearing performance. In Fig. 19 (a), note that the larger pressure tap diameter results in a larger attitude angle and smaller eccentricity ratio for the test results, though the attitude angles in the $D_t = 8mm$ set at higher speeds show some inconsistency. Similar trends can be seen in calculation results, while it is evident that there is a magnitude difference between the test and calculation results. The test results show a more downward locus and a smaller attitude angle which probably caused by the deterioration of lubrication property of lubricating oil, the temperature recorded was up to 87℃ in $D_t = 8mm$ set at higher speed, the overheated lubricating oil reduces the bearing capacity. The maximum average floating height deriving by the maximum tilting angle of the pad can prove this again. As Fig. 19 (b) shows, the larger pressure tap diameter responds to the larger maximum average floating height, the shaft did move upward by enlarging the tap diameter.

In the present work, the loading was kept constant for each set of tests, so the load capacity of the bearing could be measured by the eccentricity (ratio), a smaller eccentricity (ratio) would clearly indicate higher load capacity.

5.3. Effect of the recess area ratio

In this section, the pads with different recess areas ratios are tested. Here a dimensionless parameter, recess area ratio, is defined to represent the ratio of the recess area to the outer face area of the pad, namely $A_{ratio} = A_{recess}/A_{pad}$. Fig. 20 schematically shows the tested recess area ratios, the pressure tap diameter is 6 mm in this case. Other than that, the rest design parameters of the pad are identical.

Fig. 21 details the recess pressure for different recess area ratios. For a certain recess area ratio, the recess pressure increases at a lower speed from 448 to 1073 *RPM*, and then keep a constant at higher speed from 1800 to 3300 *RPM*. Similar trends but of different magnitude can be seen in the other two sets and the larger recess area results in a slightly lower recess pressure. The numerical results show good consistency with the test results. It is clear that the larger recess area will enlarge the integral area of recess and the recess pressure is relatively greater than the pressure distributing on other outer surfaces of the pad so that the resultant torque caused by hydrostatic oil film increases. To obtain torque equilibrium, the decrease of recess pressure leads to the decrease

Fig. 15. Distribution of oil film (a) Hydrodynamic oil film (b) Hydrostatic oil film
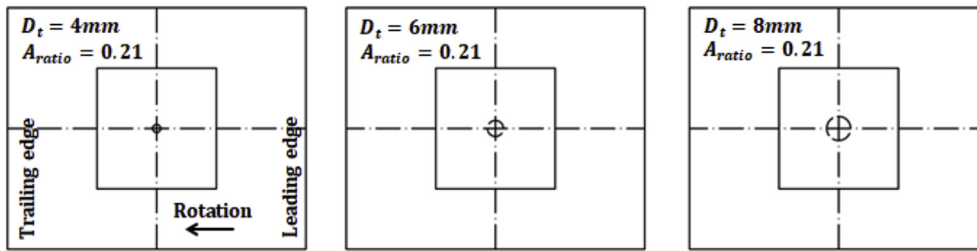$D_t = 6mm, = 0.21, = 6800N, = 3300RPM. \mu = 0.0101Pa. s$

Fig. 16. Test pad with different pressure tap diameters.

Fig. 17. Recess pressure of lower pad (*SP1*) for different pressure tap diameters.

Fig. 18. Average floating height of displacement measure points C&D for different tap diameters.

of the resultant torque caused by the hydrostatic oil film.

In Fig. 22, for the test results, the average floating heights have no change for the range of speed even though recess area ratios are different, the negative average floating height shows the no one-sided floating state at 448 *RPM*. Similar trends and magnitude can be found in calculation results.

Moreover, the constant average floating height responds to the constant tilting angle of the pad, which means the performance of bearing stay no change. As Fig. 23(a) shows, the test results of the locus basically overlap for different recess area ratios and calculation results show the same trends, the discrepancy between the test and calculation results can be explained by the deterioration of lubrication property of lubricating oil. The maximum average floating heights are given as an auxiliary proof that the bearing capacity remains constant as Fig. 23(b) shows.

Comparing with the effect of the pressure tap diameter, recess area ratio has an influence on recess pressure, while shows no effect on the tilting angle of pad. This probably because when we change recess area ratio, the flow equilibrium is still kept, while the resultant torque no more is zero, for a torque re-equilibrium, the recess pressure decreases. Note that the recess pressure decreases by 0.034 *MPa* and 0.03 *MPa* on average responding to the recess area ratio increases from $A_{ratio} = 0.18$ to $A_{ratio} = 0.21$ and from $A_{ratio} = 0.21$ to $A_{ratio} = 0.24$, respectively. On the one hand, the decrease of recess pressure barely has no influence on flow on a pressure tap scale ($D_t = 6mm \sim 8mm$) and the flow equilibrium is still kept. On the other hand, the decrease of recess pressure
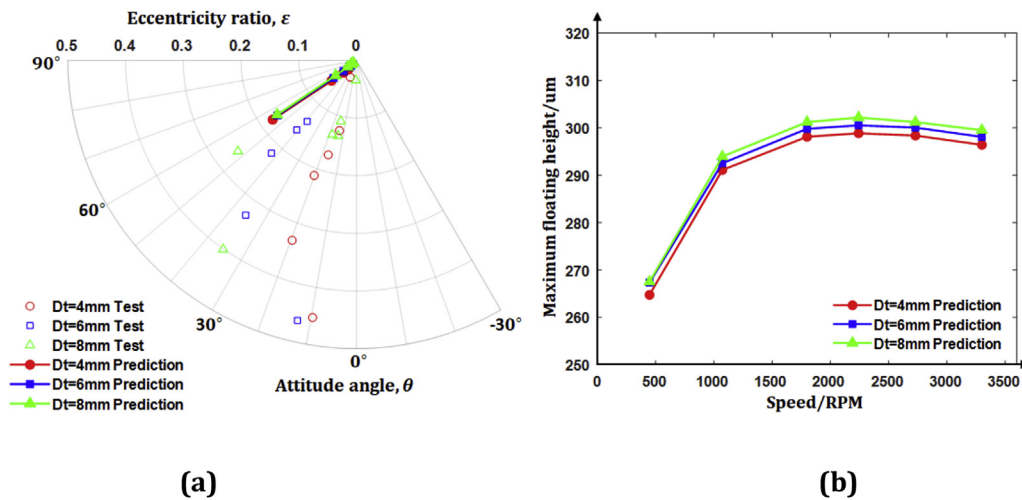
Fig. 19. (a) Locus and (b) Maximum floating height at displacement measure point C&D for different tap diameters.
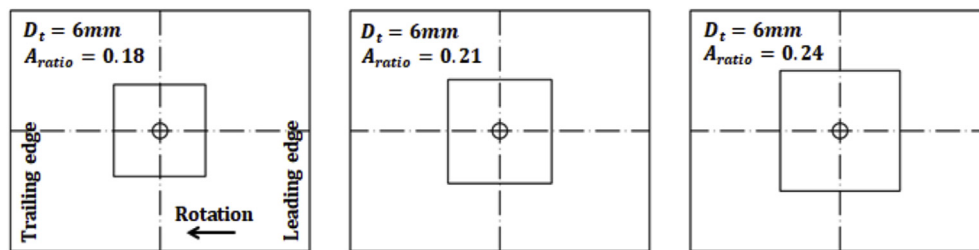

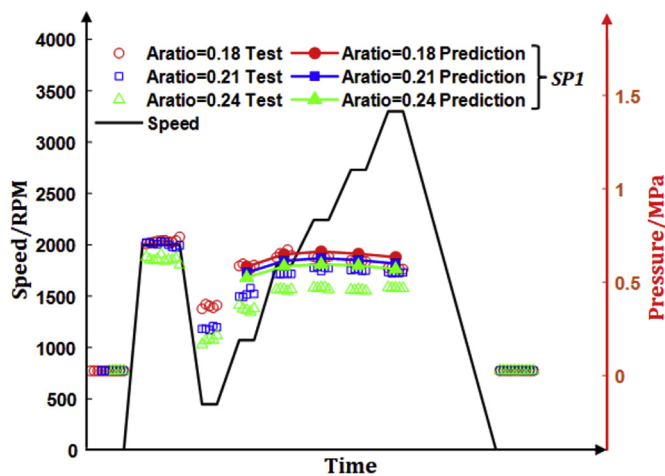**Fig. 20.** Test pad with different recess area ratios.

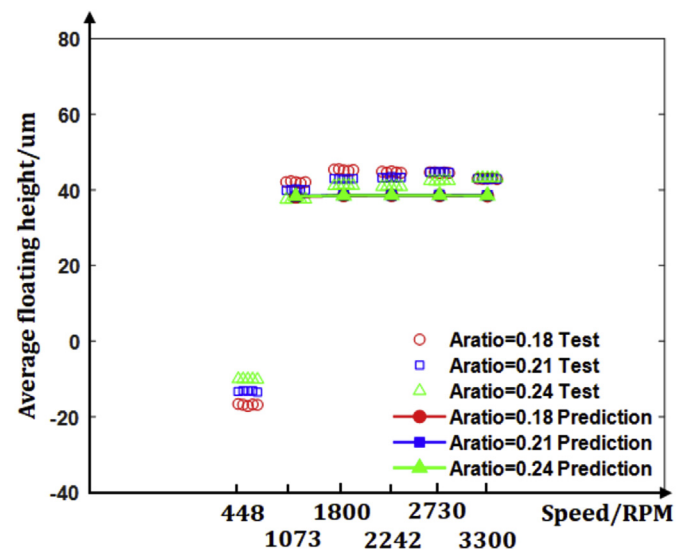**Fig. 21.** Recess pressure of lower pad (*SP1*)for different recess area ratios.

affects a lot on torque on recess area scale ($\approx 70mm$) resulting in a decrease of the increased resultant hydrostatic torque caused by the enlargement of the recess area ratio.

6. Conclusions

This series of test was performed with fluid pivot journal bearing using a full-scale bearing test rig to compare the effect of pressure tap diameter and recess area ratio of the pad on bearing performance. The one-sided floating state of the lower pad was confirmed under the given design parameters and operation conditions, while the upper two pads showed the no floating state thus acted as the fixed lobes. Based on the one-floating state model, the numerical program was established according to the one-sided floating state model. The numerical results

Fig. 22. Pad tilting angle for different recess area ratios.

were calculated to draw a comparison with the test results, which shows a good agreement with the test results. Based on the obtained results, the following conclusion can be drawn:

(1) The existence of the squeeze-film between the pad and the bearing house was demonstrated, the downward displacement of the pad was detected experimentally. And the higher speed results in the larger downward displacement.
(2) In the one-sided floating state, for a certain pressure tap diameter and recess area ratio, the recess pressure increases at lower speed from 448 *RPM* to 1800 *RPM* and remains constant at a higher speed
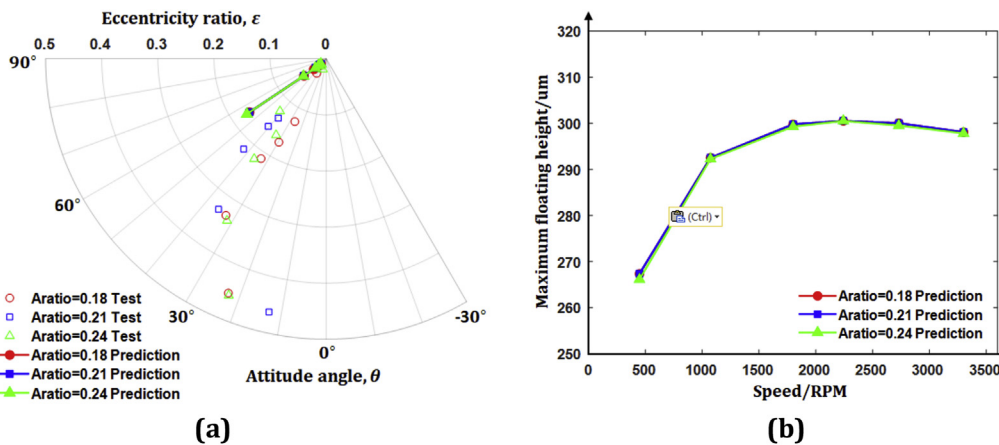
Fig. 23. (a) Locus and (b) the maximum floating height at displacement measure points C&D for different recess area ratios.

from 2242 *RPM* to 3300 *RPM*. While the tilting angle almost has no change with the increase of speed from 448 *RPM* to 3300 *RPM*.

(3) For the effect of design parameters, the different pressure tap diameters do not change the recess pressure but affect the tilting angle of the pad, the larger pressure tap diameter responds to the larger tilting angle, which leads to an increase of bearing capacity. While the different recess area ratio has an influence on recess pressure but has no influence on the tilting angle of the pad. The larger recess area ratio results in the smaller recess pressure. Because the pad tilting angle keeps constant, the loading capacity of the bearing remains constant.

(4) It is necessary to address that the recess pressure and the floating heights of each displacement measuring point are the key data to determine the floating state of the pad and to calculate the bearing performance. However, in the measurement of floating height, the kind of non-parallelism between the axis of the eddy current probe and the radial direction of the pad at the corresponding measure point results in a predictable error. Through the extensive test, these errors have been controlled with a relatively small range, the more accurate measurement methods should be proposed.

Acknowledgement

References

[1] Dimond T, Younan A, Allaire P. A review of tilting pad bearing theory. Int J Rotating Mach 2011;2011:1–23.
[2] Santos IF, Russo FH. Tilting-pad journal bearings with electronic radial oil injection. ASME J Tribol 1998;120(3):583–94.
[3] Varela AC, Nielsen BB, Santos IF. Steady state characteristics of a tilting pad journal bearing with controllable lubrication: comparison between theoretical and experimental results. Tribol Int 2013;58:85–97.
[4] Deckler DC, Veillette RJ, Choy FK. Modeling of a controllable tilting pad bearing. Proceedings of the 1997 American control conference. Albuquerque: America; 1997. p. 3416–20.
[5] Deckler DC, Veillette RJ, Braun MJ. Modeling and control design for a controllable bearing system. Proceedings of the 39th IEEE conference on decision and control, sydney, austrilia. 2000. p. 4066–71.
[6] Liu W, Feng K, Lyu P. Bifurcation and nonlinear dynamic behaviours of a metal mesh damped flexible pivot tilting pad gas bearing system. Nonlinear Dynam 2018;91(1):655–77.
[7] Wang J, Meng G. Experimental study on stability of an MR fluid damper-rotor-journal bearing system. J Sound Vib 2003;4(262):999–1007.
[8] Forte P, Paternò M, Rustighi E. A magnetorheological fluid damper for rotor applications. Int J Rotating Mach 2004;10(3):175–82.
[9] Ghaednia H, Ohadi A. Vibration behavior of flexible rotor system mounted on MR squeeze film damper with thermal growth effect. J Vib Acoust 2012;134(1):011015.
[10] Hemmatian M, Ohadi A. Sliding mode control of flexible rotor based on estimated model of magnetorheological squeeze film damper. J Vib Acoust 2013;135(5):051023.
[11] Ferfecki P, Zapoměl J, Kozánek J. Analysis of the vibration attenuation of rotors supported by magnetorheological squeeze film dampers as a multi-physical finite element problem. Adv Eng Software 2017;104:1–11.
[12] Irannejad M, Ohadi A. Vibration analysis of a rotor supported on magnetorheological squeeze film bearing with short bearing approximation: a contrast between short and long bearing approximations. J Vib Control 2017;23(11):1792–808.
[13] Zarzour M, Vance J. Experimental evaluation of a metal mesh bearing damper. J Eng Gas Turbines Power 2000;122(2):326–9.
[14] Hirani H. Stiffness and damping coefficients for rubber mounted hybrid bearing. Lubr Sci 2014;26(5):301–14.
[15] Singh OP, Sreenivasulu T, Kannan M. The effect of rubber dampers on engine's NVH and thermal performance. Appl Acoust 2014;75:17–26.
[16] Faris WF, Khalid AA, Albagul A. Experimental investigation of the dynamic response of squeeze film dampers made of steel and glass/epoxy. Shock Vib 2008;15(6):631–7.
[17] Khalid AA, Albagul A, Faris W. An experimental study on steel and Teflon squeeze film dampers. Shock Vib 2006;13(1):33–40.
[18] Faris WF, Khalid AA, Albagul A. Investigation of the performance of a rotor-bearing system containing composite and non-composite squeeze film dampers. Mater Des 2012;34:340–5.
[19] Cookson RA, Kossa SS. The vibration isolating properties of uncentralized squeeze-film dampers supporting a flexible rotor. J Eng Power 1981;103(4):781–7.
[20] Della Pietra L, Adiletta G. The squeeze film damper over four decades of investigations. Part I: characteristics and operating features. Shock Vib Digest 2002;34(1):3–26.
[21] Adiletta G, Della Pietra L. The squeeze film damper over four decades of investigations. Part II: rotordynamic analyses with rigid and flexible rotors. Shock Vib Digest 2002;34(2):97–126.
[22] Arauz GL, San Andrés L. Experimental force response of a grooved squeeze film damper. Tribol Int 1997;30(1):77–86.
[23] Jeung SH, San Andrés L, Bradley G. Forced coefficients for a short length, open ends squeeze film damper with end grooves: experiments and predictions. J Eng Gas Turbines Power 2016;138(2):022501.
[24] San Andrés L. Force coefficients for a large clearance open ends squeeze film damper with a central feed groove: experiments and predictions. Tribol Int 2014;71:17–25.
[25] San Andrés L, Diaz SE. Flow visualization and forces from a squeeze film damper operating with natural air entrainment. ASME J Tribol 2003;125(2):325–33.
[26] San Andrés L, Delgado A. Identification of force coefficients in a squeeze film damper with a mechanical end seal—centered circular orbit tests. ASME J Tribol 2007;129(3):660–8.
[27] Hollingsworth LW, inventor, Pioneer Motor Bearing Co, assignee. Hydrostatically supported tilting pad journal bearing. United State patent US 1970 Dec 22;3. 549,215.
[28] Hollingsworth LW. Inventor; Pioneer Motor Bearing Co, assignee. Hydrostatically supported tilting pad journal bearing improvements. United State patent US 1977 Nov 22;4(059):318.
[29] Messmer GA. Inventor; Pioneer Motor Bearing Co, assignee. Hydrostatically supported tilting pad journal bearing improvements. United State patent US 2000 Apr 18;6(050):727.
[30] Nelson DV, Hollingsworth LW. The fluid pivot journal bearing. ASME J Tribol 1977;99(1):122–7.
[31] Desbordes H, Fillon M, Frene J. The effects of three-dimensional pad deformations on tilting-pad journal bearings under dynamic loading. ASME J Tribol 1995;117(3):379–84.
[32] Kim SG, Kim KW. Influence of pad–pivot friction on tilting pad journal bearing. Tribol Int 2008;41(8):694–703.
[33] Harangozo AV, Stolarski TA, Gozdawa RJ. The effect of different lubrication methods on the performance of a tilting-pad journal bearing. Tribol Trans 1991;34(4):529–36.
[34] Coghlan DM, Childs DW. Characteristics of a spherical-seat TPJB with four methods of directed lubrication—Part I: thermal and static performance. J Eng Gas Turbines

Power 2017;139(12):122502.

[35] Coghlan DM, Childs DW. Characteristics of a spherical seat TPJB with four methods of directed lubrication—Part II: rotordynamic performance. J Eng Gas Turbines Power 2017;139(12):122503.

[36] Harangozo AV, Stolarski TA. Fundamental dynamic performance of fluid-pivot and squeeze-film damper bearings. Tribol Int 1993;26(6):413–9.

[37] Singh AK, Mukherjee PS, Mishra NM. Interrelationship among viscosity, temperature and age of lubricant. Ind Lubr Tribol 2006;58(1):50–5.

[38] Khonsari MM, Booser ER. Applied tribology: bearing design and lubrication. 3th ed. John Wiley & Sons; 2017.

[39] Dowson D. A generalized Reynolds equation for fluid-film lubrication. Int J Mech Sci 1962;4(2):159–70.

[40] Wang N, Chang SH, Huang HC. Stopping criterion in iterative solution methods for Reynolds equations. Tribol Trans 2010;53(5):739–47.